npj | computational materials

Article

Published in partnership with the Shanghai Institute of Ceramics of the Chinese Academy of Sciences

https://doi.org/10.1038/s41524-024-01467-4

Sub-bandgap charge harvesting and energy up-conversion in metal halide perovskites: ab initio quantum dynamics

Bipeng Wang[1], Weibin Chu[2,3], Yifan Wu[2], Wissam A. Saidi[4,5] & Oleg V. Prezhdo[2,6]

Metal halide perovskites (MHPs) exhibit unusual properties and complex dynamics. By combining ab initio time-dependent density functional theory, nonadiabatic molecular dynamics and machine learning, we advance quantum dynamics simulation to nanosecond timescale and demonstrate that large fluctuations of MHP defect energy levels extend light absorption to longer wavelengths and enable trapped charges to escape into bands. This allows low energy photons to contribute to photocurrent through energy up-conversion. Deep defect levels can become shallow transiently and vice versa, altering the traditional defect classification into shallow and deep. While defect levels fluctuate more in MHPs than traditional semiconductors, some levels, e.g., Pb interstitials, remain far from band edges, acting as charge recombination centers. Still, many defects deemed detrimental based on static structures, are in fact benign and can contribute to energy up-conversion. The extended light harvesting and energy up-conversion provide strategies for design of novel solar, optoelectronic, and quantum information devices.

Far-from-equilibrium, excited state processes are key to a broad range of modern applications, ranging from solar energy harvesting, to optoelectronics, quantum information processing, and medicine[1–7]. Further progress relies on ability to model the processes on the atomistic level, capturing realistic aspects of system structure associated with defects, interfaces, surfaces, etc. A methodology of choice should capture the highly non-equilibrium nature of the evolution of coupled electronic, vibrational, spin and other relevant degrees of freedom. A combination of real-time time dependent density functional theory (TDDFT) and nonadiabatic (NA) molecular dynamics (MD) provides the desired framework[8–19], as it mimics nature in the most direct way, and allows one a detailed modeling of time-resolved spectroscopy measurements performed by experimentalists to elucidate excited state dynamics in a broad range of systems. NAMD/TDDFT calculations carry a high computational cost that should be reduced to make the approach applicable to new classes of systems and problems.

Metal halide perovskites (MHPs) is a modern material with complex electron-vibrational dynamics and a great potential for solar energy, optoelectronic and other applications because of their favorable optical and electronic properties[20–28]. The intrinsically strong light absorption, tunable bandgap, long charge carrier lifetimes, efficient carrier transport, and low manufacturing cost appeal highly to investigators from both academia and industry. Since the first reported MHP solar cell in 2009[29], the power conversion efficiency has risen rapidly from 3.8% to 26%[30,31]. MHPs covers a large family of compounds with the general formula ABX_3, where A is either an organic cation, e.g., $CH_3NH_3^+$ and $CH(NH_2)_2^+$, or an inorganic cation, e.g., Cs^+, B is a metal cation, such as Pb^{2+}, Sn^{2+} and Ge^{2+}, and X is a halide anion, including Cl^-, Br^- and I^-. MHPs exhibit simultaneously features of inorganic, organic and even liquid matter: The periodic inorganic lattice ensures efficient charge transport. Similar to organic matter, MHPs undergo a variety of photochemical reactions, and analogies can be drawn between large polarons in MHPs and ion solvation in liquids[32–35]. MHPs are much softer than typical commercial inorganic semiconductors, such as Si, GaAs, and TiO_2, as characterized by Young's modulus. The complex composition and geometric structure of MHPs, combined with the softness, give rise to significant structural fluctuations over a variety of time scales[34,36–40]. It is important to model geometric changes and fluctuations in MHPs because they intimately couple to and have a significant impact on the electronic properties and charge carrier transport and lifetime[41]. While ab initio NAMD/TDDFT calculations provide essential insights into the electronic and structural dynamics of MHPs, they are computationally demanding.

[1]Department of Chemical Engineering, University of Southern California, Los Angeles, CA, 90089, USA. [2]Department of Chemistry, University of Southern California, Los Angeles, CA, 90089, USA. [3]Key Laboratory of Computational Physical Sciences (Ministry of Education), Institute of Computational Physical Sciences, Fudan University, Shanghai, 200433, People's Republic of China. [4]Department of Mechanical Engineering & Materials Science, University of Pittsburgh, Pittsburg, PA, 15260, USA. [5]National Energy Technology Laboratory, United States Department of Energy, Pittsburgh, PA, 15236, USA. [6]Department of Physics and Astronomy, University of Southern California, Los Angeles, CA, 90089, USA. e-mail: prezhdo@usc.edu

Further computational advances are needed for exploration of electron-vibrational dynamics of complex systems.

Machine learning (ML) has arisen as a powerful tool to provide an efficient and accurate interpolation of complex sets of data[42–46]. It is now widely used to develop force fields (FFs) based on input obtained by ab initio methods[47–49]. Providing ab initio level accuracy, MLFFs are much more computationally efficient and can be used to generate nano- and micro-second trajectories for systems composed of thousands of atoms. MLFFs are capable of tracking structural evolution of MHPs on the timescales comparable to the charge carrier lifetimes[38–40]. In addition to the proper sampling of structural evolution, NAMD simulations require calculation of electronic properties, in particular, electronic state energies and couplings between the states, including NA, Coulomb, spin-orbit, and optical transition dipole matrix elements. Evaluation of the electronic properties can be assisted by ML as well. One can develop ML models of electronic Hamiltonians[19,50,51]. Alternatively, one can calculate the electronic properties ab initio, along MLFF trajectories but over large timesteps, and then interpolate for the intermediate times[52–54]. The input provided by the ML models of electronic and structural properties, trained based on ab initio data, can then be used perform NAMD simulations of excited state processes in systems perturbed far from thermodynamic equilibrium.

In this work, we report a quantum dynamics simulation methodology that integrates ML, time-independent and TDDFT, and NAMD. The approach enables one to study excited state dynamics in condensed phase and nanoscale systems over nanosecond timescales, comparable to excited state lifetimes. Using this methodology, we investigate structural and optical properties and excited state dynamics in the best known $MAPbI_3$ MHP containing four common defects: I vacancy (I_v), I interstitial (I_i), Pb interstitial (Pb_i), and MA replacement with I (MA_I). We show that thermal structural fluctuations result in large, up to 1 eV fluctuations in mid-gap defect levels, giving rise to sub-bandgap light absorption. The majority of the defect levels approach band edges, allowing charges to escape into bands and resulting in energy up-conversion. The I_v, Pb_i and MA_I defects extend the absorption spectrum into the infrared region, while the I_i defect enhances absorption near the band edge. The energy up-conversion is possible with the I_v, I_i and MA_I defects. The energy level of the Pb_i defect also exhibits a large fluctuation; however, it never approaches band edges, acting as an efficient charge recombination center. Therefore, Pb_i defect passivation strategies are required. Fluctuations of the energy levels of the I_v defect occur on a 100 ps timescale, showcasing the value of the developed ML-based NAMD simulation methodology, allowing one to investigate long-time dynamics and rare events. The reported findings provide valuable insights for designing next-generation materials with improved light-harvesting and energy conversion properties for solar cell and optoelectronic applications.

Results

Electronic and geometric structure at 0 K

The upper panel of Fig. 1 shows the optimized structures of pristine $MAPbI_3$ and its defective variants, with each defect highlighted for clarity, Fig. 1b–e. It is instructive to study the static (0 K) electronic structure of these systems before delving into the complex dynamics of charge trapping and recombination. The MA_I and Pb_i defects introduce mid-gap trap states near the conduction band minimum (CBM), approximately 0.5 eV below the CBM. In comparison, the I_i defect creates a mid-gap trap state located near the valence band maximum (VBM), around 0.1 eV above the VBM. Notably, no trap state is observed in the optimized I_v structure due to the equilibrium distance between two Pb atoms across the vacancy equal to 6.05 Å, which is sufficiently long to prevent trap state formation. The lower panels in Fig. 1 present the projected densities of states (DOS) for each configuration. The results indicate that iodine atoms predominantly contribute to the VBM, while lead atoms are the primary contributors to the CBM. The calculated energy gaps between the VBM and CBM for the pristine and defective systems are 1.79 eV, 1.82 eV, 2.01 eV, and 1.62 eV, respectively. These static calculations provide important insights into the electronic structure of $MAPbI_3$ and its defective forms. However, the static limit at 0 K does not fully capture the dynamical behavior of defect states at ambient and operating conditions. Finite temperature analysis is critical for understanding charge carrier properties.

Sub-bandgap charge harvesting by dynamic defects at ambient temperature

Figure 2 presents evolution of the band edges and defect levels at ambient temperature (300 K), highlighting the influence of thermal vibrations in MHPs. Due to the inherent softness of MHPs, thermal fluctuations play a critical role in determining the dynamical behavior of the defect states. The deep trap states created by the MA_I and Pb_i defects at 0 K, undergo significant fluctuations at 300 K, Fig. 2a,b. The fluctuations span approximately 0.9 eV for MA_I and 0.5 eV for Pb_i, bringing the trap states closer to the CBM. The MA_I level frequently becomes quasi degenerate with the CBM, providing a favorable condition for trapped charges to escape to the CBM via thermal excitation. In contrast, the Pb_i level never approaches the CBM sufficiently close to allow the thermal escape, indicating that the Pb_i defect acts as a charge recombination center. The I_i defect level does not exhibit large fluctuations and remains close to the VBM, Fig. 2c. This facilitates

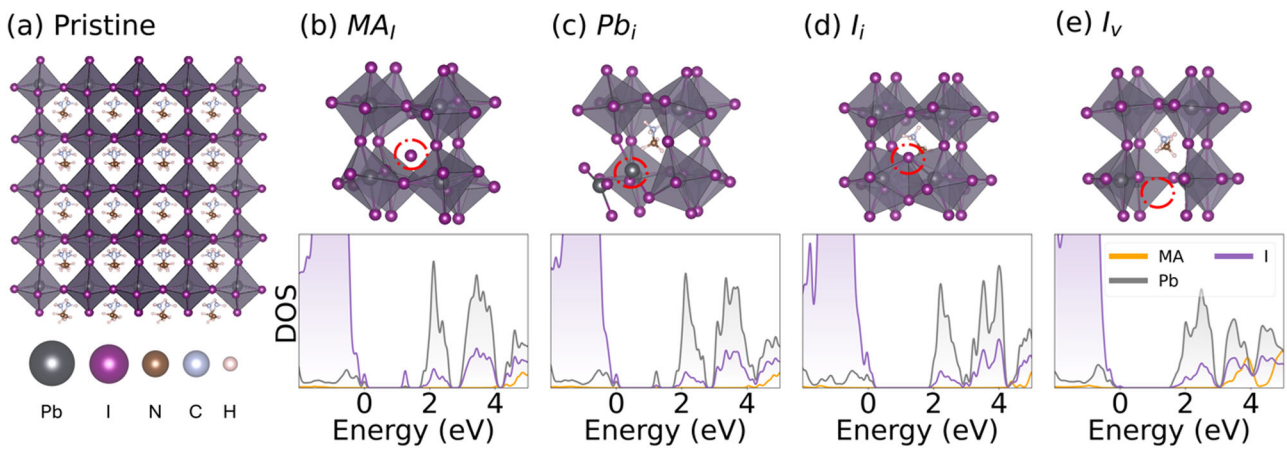

Fig. 1 | Geometric and electronic structures of systems under investigation. **a** Optimized geometry of pristine $MAPbI_3$. Defects are created by modifying the pristine structure. **b**–**e** Detailed view of the optimized geometries with MA_I replacement, Pb_i interstitial, I_i interstitial, and I_v vacancy defects, along with the corresponding density of states (DOS). Zero energy is set to the VBM. The MA_I, Pb_i, and I_i defects induce mid-gap trap states. The I_i trap state is close to the VBM. There are no mid-gap states in the optimized structure of the I_v defect, because distance between the Pb atoms across the vacancy is 6.05 Å. The distance decreases at ambient temperature, allowing p-orbitals of the Pb atoms to overlap and give rise to mid-gap trap states, Figs. 2d and 3.

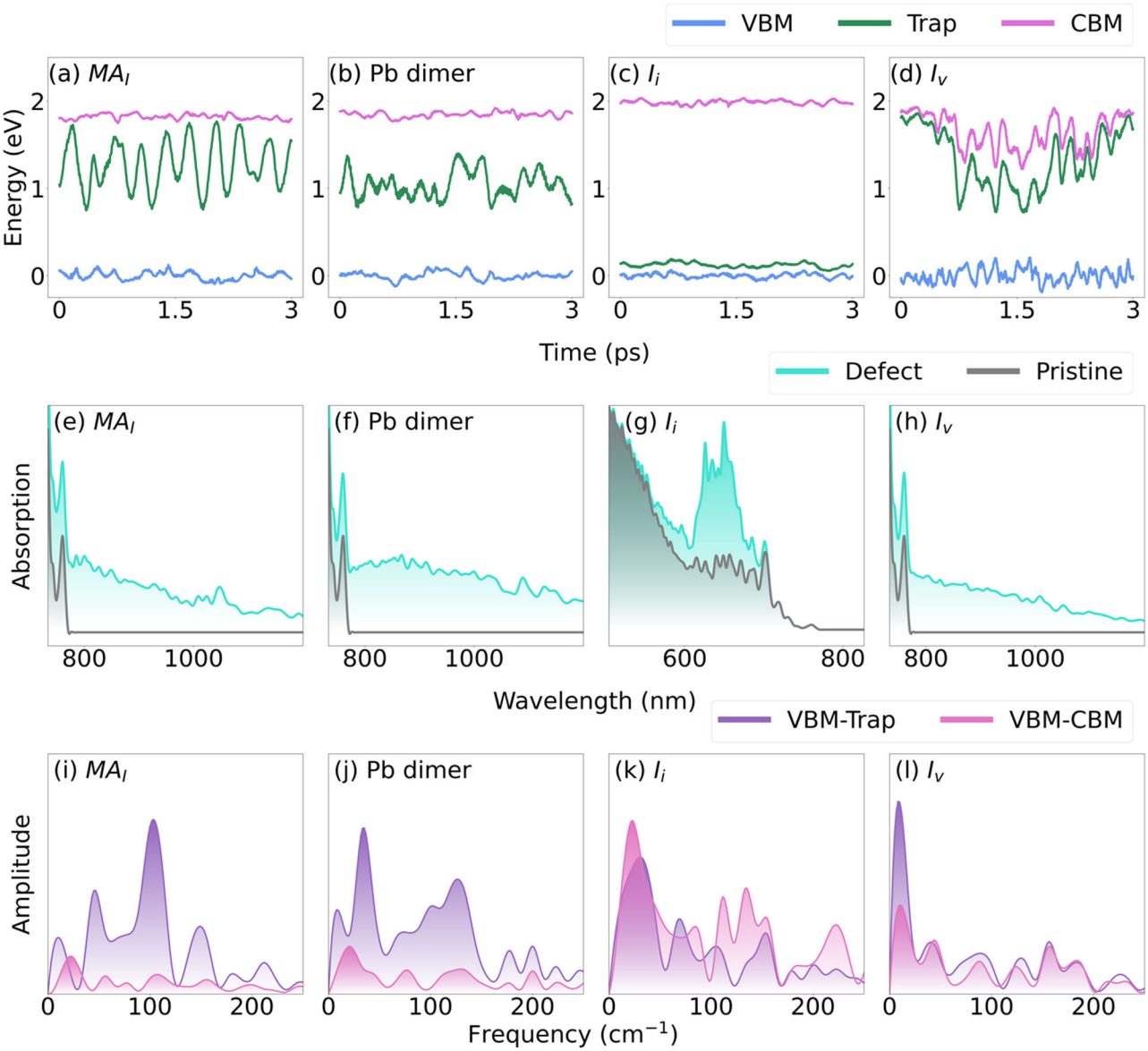

Fig. 2 | Evolution of the VBM, CBM, and defect levels in $MAPbI_3$ at ambient temperature. a MA_I replacement, (**b**) Pb_i interstitial, (**c**) I_i interstitial, and (**d**) I_v vacancy. Defect levels fluctuate significantly, often approaching band edges. Optical absorption of $MAPbI_3$ with (**e**) MA_I, (**f**) Pb_i, (**g**) I_i, and (**h**) I_v relative to the absorption of pristine $MAPbI_3$. All defects enhance absorbance at long wavelengths, either below (MA_I, Pb_I, I_v) or at (I_i) the bandgap. **i–l** Fourier transforms of fluctuations of the VBM-CBM and VBM-trap (MA_I, Pb_I, I_v) or trap-CBM (I_i) energy gaps, identifying the vibrational modes coupled to the electronic subsystem. Trap levels exhibit stronger electron-vibrational coupling than band levels.

mixing of the localized defect level wavefunction with delocalized band states, and allows thermal excitation of charges from the defect level into the band. The part of the trajectory of the I_v defect level shown in Fig. 2d is derived from a nanosecond-long MLMD simulation analyzed in more detail below. Deep trap states appear when the two Pb atoms across the I_v vacancy approach each other. The Pb-Pb dimer forms spontaneously on a 100 ps timescale[38], and can be stabilized by vacancy charging during device operation[55]. Several mid-gap levels can form as a result of the Pb-Pb dimer formation, with the lowest level dropping by 1 eV below the CBM.

Next, we compute the absorption spectra for the pristine and defective $MAPbI_3$ systems at 300 K by calculating the transition dipole moments within the Franck-Condon approximation and averaging over several hundred structures from the MD trajectories, Fig. 2e–h. Pristine $MAPbI_3$ exhibits strong cross-bandgap absorption at wavelengths below 750 nm, resulting in photo-induced charge carrier generation in the visible region. The spectral signal grows at shorter wavelengths, indicating efficient above-bandgap absorption. The exponential Urbach tail extending from 750 nm to 800 nm in pristine $MAPbI_3$, just below the bandgap, is attributed to thermal phonon-induced absorption. However, sub-bandgap absorption is very limited in pristine $MAPbI_3$, highlighting its limitations in generating photo-induced charge carriers in the sub-bandgap region and energy up-conversion. In contrast, Fig. 2e, f, h demonstrate that MA_I, Pb_i, and I_v defects significantly enhance sub-bandgap absorption, particularly in the region beyond 800 nm. It is important to note that the sub-bandgap absorption described here excludes multi-photon processes. We emphasize that dynamic, defect-induced photo-absorption cannot be captured by a static model of the optimized geometry at 0 K. The extended absorption beyond 800 nm in systems with the MA_I, Pb_i, and I_v defects arises from optical transitions between the valence band and dynamically fluctuating defect levels. This sub-bandgap absorption extends deep into the infrared region, which aligns with the amplitude of the dynamic defect level fluctuations seen in Fig. 2a, b, d, suggesting the possibility of energy up-

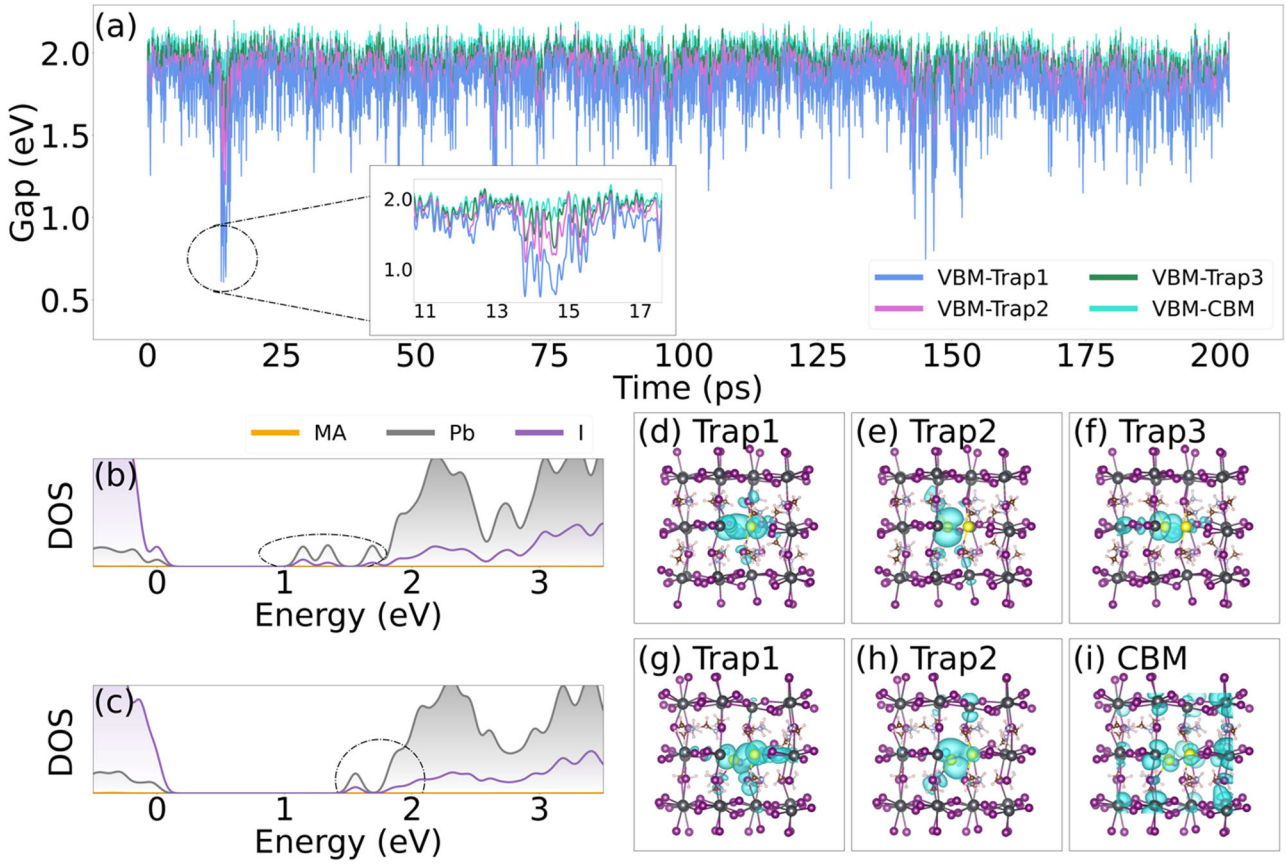

Fig. 3 | Electronic states in $MAPbI_3$ with I_v vacancy at ambient temperature. **a** Evolution of energy gaps between the VBM and the three states above it in $MAPbI_3$ with I_v vacancy over 200 ps. The insert exemplifies a region with deep traps. **b**, **c** Projected DOS for structures exhibiting 3 and 2 localized trap states indicated by the dashed ovals. The corresponding charge densities are shown in (**d**–**f**) and (**g**–**i**). The distance between the two Pb atoms (highlighted in yellow) across the vacancy is 3.58 Å in part (**b**, **d**–**f**) and 3.86 Å in part (**c**, **g**–**i**).

conversion. Although the intensity at large wavelengths is relatively weak, due to the optical transition occurring between delocalized band states and the localized trap states, light absorption remains possible in the red and infrared regions of defective $MAPbI_3$. In comparison, longer wavelength absorption is typically achieved in the conventional semiconductors through heavy doping, where overlapping dopant wavefunctions form intermediate bands[56]. The I_i defect enhances the cross-bandgap absorption, as its defect level remains close to the VBM, limiting its impact on sub-bandgap absorption, Fig. 2c, g.

Figure 2i–l presents Fourier transforms (FTs) of the phonon-induced fluctuations of the energy gaps between trap and band states in the defective systems, compared to the VBM-CBM FT in pristine $MAPbI_3$. All systems exhibit strong signals at low frequencies below 200 cm^{-1}. The intensities are higher for transitions involving defect levels compared with the bandgap transition, because the defect energy levels are influenced by structural motions much more strongly than band states, Fig. 2a, b, d. The I_i defect constitutes an exception, Fig. 2k. Its influence spectrum is similar to that of pristine $MAPbI_3$, because the I_i defect level is close to the VBM, and the I_i level and the VBM fluctuate in similar ways.

Prior work[57] has demonstrated that trap states contribute bright spectral features to the optical absorption, while accelerating charge recombination only slightly, creating favorable conditions for the sub-bandgap light-harvesting. It should be noted that the behavior of point defects on surfaces, interfaces and grain boundaries can differ from that in the bulk[40,58]. Still, the qualitative features, such as the large amplitude defect level fluctuations, should be present in nanostructures of different dimensionalities, since structural softness and ionic character are general to MHPs.

A detailed analysis of the properties of the I_v vacancy defect system over a 200 ps timescale is presented in Fig. 3. Significant fluctuations in the electronic energy levels are observed on a 50–100 ps time scale. Several times during the 200 ps trajectory trap levels appear deep inside the bandgap, and up to 3 trap levels can form. Such fluctuations cannot be captured with short ab initio MD trajectories that are limited to about 10 ps. The inset in Fig. 3a shows a region with 3 trap levels on a finer scale and contains the clip discussed in Fig. 2d. The energies of the trap levels correlate with the distance between the two Pb atoms across the iodine vacancy. The distance oscillates by several Angstroms at room temperature. The 6.05 Å Pb-Pb distance in the optimized structure decreases to 3.42. Å in the deep trap region. As the Pb-Pb distance decreases via a spontaneous fluctuation driven by low frequency acoustic modes, the p_x-orbitals, pointing along the direction between the two Pb atoms, start overlapping, and the first trap state is formed. As the distance decreases further, two more trap states are formed, involving p_y- and p_z-orbitals of the two Pb atoms. Figure 3b, c shows DOS and trap state charge densities for representative structures containing 2 and 3 trap states. The appearance of the deep mid-gap states due to thermal fluctuation of the I_v defect structure extend light absorption into the red and infrared, Fig. 2h.

Charge carrier trapping, escape and recombination dynamics

Mid-gap levels extend light harvesting into sub-bandgap energy region. However, in the traditional semiconductors, high mid-gap level density is required to form an intermediate band that can facilitate charge transport[56]. Otherwise, charge carriers occupying mid-gap levels remain trapped and are eventually lost through nonradiative recombination. The large fluctuations of defect energy levels in MHPs create opportunities for the charges to

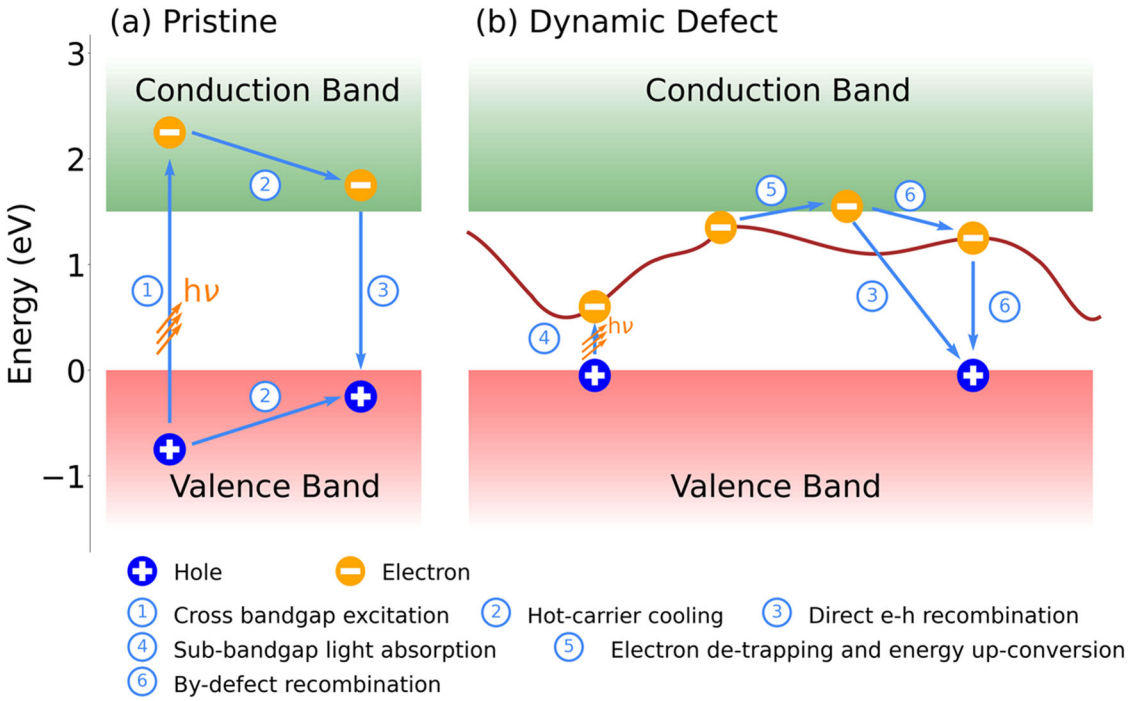

Fig. 4 | Schematic of the photophysical processes metal halide perovskites. **a** Pristine system. **b** System with dynamic defects. Photoexcitation of the pristine system above the bandgap (1) results in intraband relaxation of hot carriers (2), followed by carrier recombination (3). In a system with dynamic defects, sub-bandgap excitation (4) extends light absorption to longer wavelengths, Fig. 2e–h, and allows charges to escape into bands (5). This energy up-conversion process competes with defect assisted charge recombination (6).

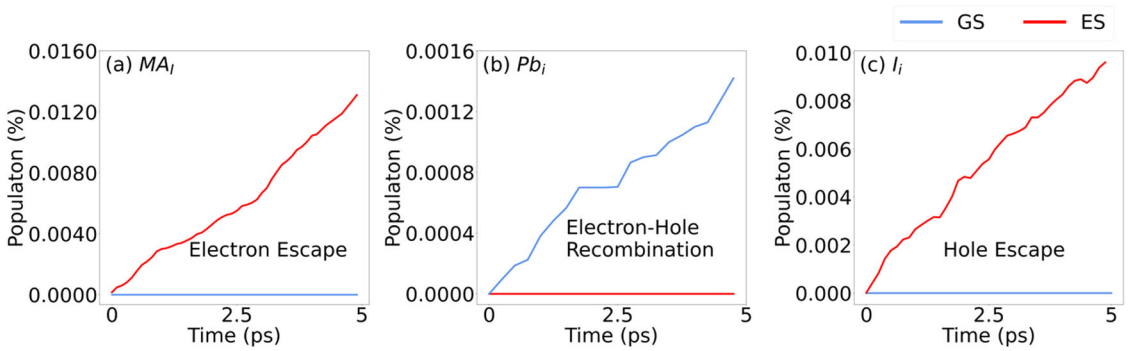

Fig. 5 | Charge carrier dynamics in $MAPbI_3$ with point defects. Shown are populations of the excited state (ES) with electron and hole at the band edges, and the ground state (GS), following photoexcitation of the defect states in $MAPbI_3$ with (**a**) MA_I, (**b**) Pb_i and (**c**) I_i defects. The corresponding data for the I_v defect are shown in Fig. 6d. Sub-bandgap excitation of MA_I, I_i and I_v defect levels results in energy up-conversion and charges escaping into bands, as indicated by growth of the ES population, because the defect levels fluctuate between shallow and deep regimes, Fig. 2a, c, d. In contrast, populating the Pb_i defect results in charge recombination, i.e., growth of the GS population, because the Pb_i defect always remains deep, Fig. 2b.

escape into the main bands, and it is important to establish whether charges do escape or are lost through nonradiative relaxation, as they are in the traditional semiconductors.

Figure 4 depicts the photoinduced processes occurring in pristine and defective MHPs. Absorption of sunlight by the pristine system, process (1) in Fig. 4a, creates charge carriers at different energies inside the valence and conduction bands. The charges relax rapidly to the band edges, process (2). Subsequently, the charges are either extracted or recombine, process (3). In addition to these processes, a system containing defects can exhibit sub-bandgap light absorption into defect levels, process (4) in Fig. 4b. The trapped charges can recombine, process (6). However, defect levels fluctuate strongly in MHPs, and the charges generated by the sub-bandgap absorption can escape into bands, process (5), and carry out electrical or chemical work.

Figures 5 and 6d present NAMD simulation results describing competition between charge escape from the trap states into bands and electron-hole recombination. The MA_I, I_i and I_v defects allow charges to escape the trap states, because the fluctuating defect levels approach the band closely, Fig. 2a, c, d. In contrast, the Pb_i defect acts as a nonradiative charge recombination center, because its energy level remains far from the band edges, even though it also fluctuates by a significant amount, Fig. 2b. The charges escaped into bands can be trapped again; however, in realistic systems with relatively low defect density, charges travel away from defects and the likelihood for the charge to be trapped by the same defect again is low. This behavior contrasts sharply with that of traditional semiconductors, where trap level fluctuations are small[37], preventing trapped charges from escaping into bands.

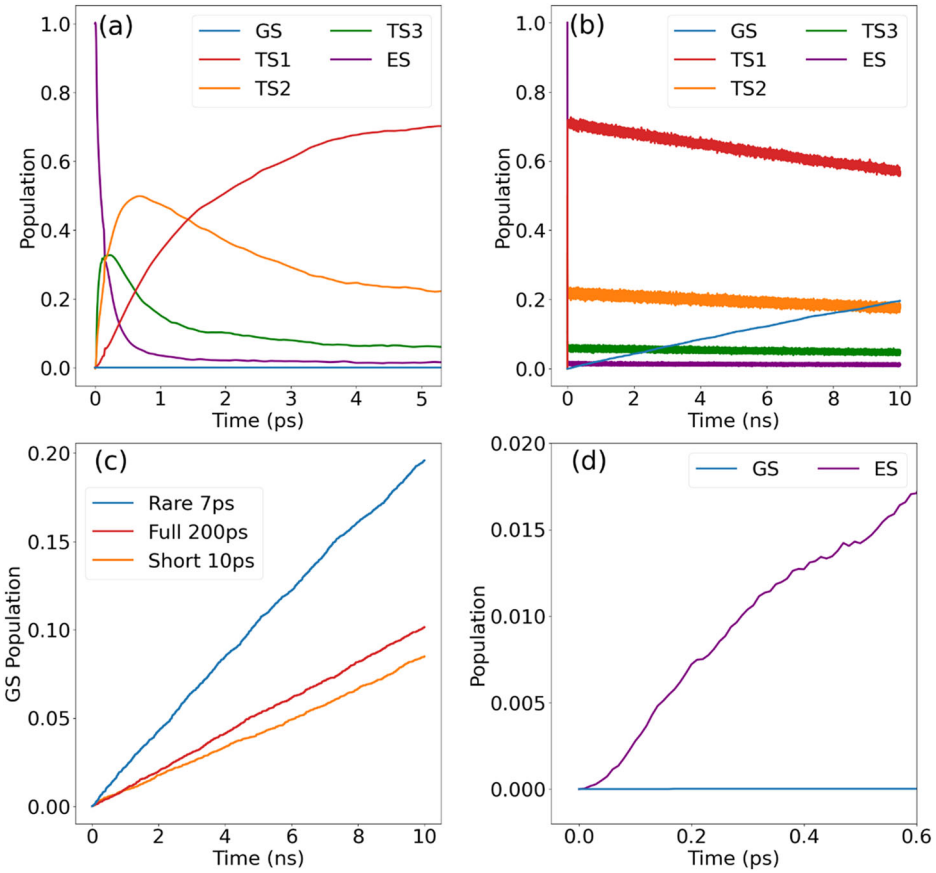

Fig. 6 | Charge carrier dynamics in $MAPbI_3$ with I_v vacancy. Shown are populations of the ground state (GS), the excited state (ES) with electrons and holes at the band edges, and the three trap states (TS1, TS2, TS3), Fig. 3. **a** Early time dynamics starting from the ES, showing charge trapping within a few picoseconds. **b** Nanosecond dynamics starting from the ES, demonstrating electron-hole recombination, i.e., growth of the GS population. **c** Comparison of electron-hole recombination simulated using the initial 10 ps, representing a typical ab initio simulation (Short 10 ps), the 7 ps including the rare event with deep traps (Rare 7 ps), insert of Fig. 3a, and the full 200 ps trajectory (Full 200 ps). The recombination accelerates when the traps are deep, and therefore, the full 200 ps data show faster recombination than the short 10 ps ab initio result. **d** Electron escape from the trap states. The trapped charge escapes into the band much faster than it decays to the GS. Corresponding data for the MA_I, Pb_i and I_i defects are shown in Fig. 5.

Figure 6 presents NAMD detailed simulation results for the I_v system. It highlights the developed capability to perform the simulations using the NAMD Hamiltonian obtained along the 200 ps trajectory, Fig. 3. Thus, we are able to investigate the influence of the rare events responsible for appearance of deep trap states on charge carrier recombination. Figure 6a demonstrates rapid, sub-ps charge trapping during the 7 ps region with the deep traps, insert in Fig. 3a. The ground state gets populated over tens of nanoseconds, Fig. 6b. Figure 6c compares charge recombination obtained using the full 200 ps NAMD Hamiltonian, the first 10 ps representing a typical ab initio simulation, and the 7 ps rare event NAMD Hamiltonian. The deep trap states appearing during the rare 7 ps event accelerate charge recombination. However, the recombination obtained with the full 200 ps trajectory is only slightly faster than the recombination for the short 10 ps trajectory, because the deep traps are formed only transiently, Fig. 2a. Thus, the argument that deep defects are detrimental to semiconductor performance does not necessarily apply to MHPs. On the contrary, as shown in Fig. 6d, obtained for the region with the deep traps, the electrons excited into the trap states can escape into the conduction band much faster than they relax to the ground state, due to the large fluctuation of the trap levels.

Many factors can lead to formation of deep defect levels in MHPs[59], including charging[55], grain boundary deformation[39,40], point defect migration[41], strain[60,61], and surface effects[62–64]. In all case, significant fluctuations of defect levels should be expected, because MHPs are soft[65] and undergo large scale anharmonic structural motions[66].

Discussion

We have reported a quantum dynamics simulation methodology that integrates NAMD, ab initio time-independent and time-dependent DFT, and ML. The approach allows one to model excited state dynamics in nanoscale, molecular and condensed matter systems over nanosecond timescales, comparable to excited state lifetimes. Proper sampling the NAMD Hamiltonian is essential to capture rare events, which occur in such systems, and influence their structural and electronic properties, and response to external stimuli. We have demonstrated the utility of developed methodology by application to the most studied $MAPbI_3$ MHP with the common I_v defect. In the optimized structure and in short ab initio trajectories at ambient temperature, the defect creates no mid-gap levels. However, on a 50–100 ps timescale, slow acoustic modes of $MAPbI_3$ bring the two Pb atoms across the I_v vacancy sufficiently close to allow their p-electron orbitals to overlap and form up to three deep mid-gap trap levels. The NAMD simulations show that charge carrier recombination is accelerated significantly during these transient events. However, overall, the recombination is accelerated by 20–30% only, because the deep charge trap levels exist only for brief periods of time.

The study demonstrated two important phenomena associated with the unusual properties of intrinsic defects in MHPs, namely, sub-bandgap light absorption and energy up-conversion. The fluctuating energy levels of intrinsic point defects span a wide energy range at ambient conditions, as demonstrated with the I_v, Pb_i and MA_I defects in $MAPbI_3$. This is in contrast with the traditional inorganic semiconductors, in which defect levels fluctuate much less. Thus, the commonly used classification of defects into shallow and deep does not fully apply to MHPs. Part of the time many defect levels approach band edges, and therefore, effectively, most defects in MHPs can be regarded as shallow. The large fluctuations of the energy levels of intrinsic defects in MHPs extend light absorption into low energies below the bandgap. Even excitations several tens of eV below the band edge can produce mobile charge carriers, because the charges can escape the defect levels when the levels approach the band edges. This has been shown by the NAMD simulations for the I_v, I_i and MA_I defects. Energy levels of some defects, such as Pb_i, never approach the band edges and act as charge recombination centers. Therefore, they should be passivated to improve MHP performance. The demonstrated mechanisms of sub-bandgap light

absorption and energy up-conversion to generate mobile charge carriers can operate at both low and high defect concentration. In comparison, high defect/dopant concentrations are needed in traditional semiconductors to form intermediate bands and produce mobile charge carriers through sub-bandgap light absorption

The long-time NAMD simulation methodology reported here provides an important tool for studying excited state processes in realistic materials. The demonstrated sub-bandgap light-harvesting and energy up-conversion mediated by intrinsic defects highlight the distinct properties of MHPs and provide guidelines for designing next-generation low-cost materials with improved performance.

Methods

Electronic structure calculations

Ab initio electronic structure calculations are performed with the Perdew–Burke–Ernzerhof (PBE)[67] density functional employing projected augmented pseudopotentials[68], and D3 van der Waals correction[69], as implemented in the Vienna Ab initio Simulation Package[70]. Spin-orbit coupling plays an important role in determining the electronic properties of MHPs, because they are composed of heavy elements. Fortunately, due to cancelation of errors associated with electron self-interaction and neglect of spin-orbit coupling, the bandgap and defect energy levels obtained for $MAPbI_3$ with the PBE functional agree with those obtained at higher levels of theory. The cutoff energy of the plane wave basis is set to 450 eV. The convergence thresholds for the energy and the forces are 10^{-7} eV and 10^{-3} eV/Å, respectively. A super cell, including 4 × 2 × 2 unit cells, is created to model $MAPbI_3$, Fig. 1. Defects are introduced into the pristine cell: the MA_I replacement defect is modeled by substituting an MA group with an iodine atom, the Pb_i interstitial defect is created by adding an extra lead atom, the I_i interstitial defect is introduced by inserting an additional iodine atom, and the I_v is modeled by removing an iodine atom. The resulting systems contain 377, 385, 385, and 383 atoms, respectively. Although the simulation cells are already rather large for the ab initio NAMD simulations, even bigger cells are desirable to achieve experimental defect concentrations. This can be achieved with ML models of electronic Hamiltonians[19]. Mid-gap trap states arising from point defect are localized, and their properties depend weakly on simulation cell size.

Machine learning force field and molecular dynamics

The MLFF is trained using the DeepPot-SE approach[71] as implemented in DeePMD-Kit[72]. The training data are generated with CP2K[73] using the PBE functional[67] with the DFT-D3 van der Waals correction[69], MOLOPT basis sets[74], and GTH norm-conserving pseudopotentials[75]. The neighbor searching is performed with a 7 Å cutoff radius and a 2 Å smoothing distance. The embedding and fitting neural networks have 25 × 50 × 100 and 240 × 240 × 240 dimensions, respectively. The network optimization is carried out using the Adam stochastic gradient descent method[76] with a learning rate that decreases exponentially from the starting value of 0.001. The training data are generated via NVT simulations at temperatures ranging from 100 K to 600 K using both pristine and defective structures. The atomistic simulations are carried out using Large-scale Atomic/Molecular Massively Parallel Simulator (LAMMPS)[77]. The structures are visualized with the VESTA software package[78].

Nonadiabatic molecular dynamics and time-domain density functional theory

To perform the NAMD/TDDFT simulations, the I_v system is heated up to 300 K, and a 3 ns microcanonical trajectory is generated with the MLFF. A randomly selected 200 ps part of the ML trajectory is analyzed ab initio and by inverse fast Fourier transform (iFFT). 3152 structures are chosen along the 200 ps trajectory every 64 fs to calculate the ab initio electronic energy levels, and 6304 structures (3152 pairs) are used to calculate the ab initio NA couplings, which are obtained as overlaps of wavefunctions at adjacent timesteps[79,80]. Computed every 64 fs, the ab initio energy levels and NA couplings are interpolated using the iFFT method[53] to generate the NA Hamiltonian with a 1 fs timestep. The I_i, Pb_i and MA_I systems are studied by ab initio MD, because their structural fluctuations occur on a picosecond timescale. The systems are heated up to 300 K, and 7 ps microcanonical trajectories are generated. The last 3 ps are used for further analysis. The NAMD calculations are performed in the Kohn–Sham representation[81]. Excitonic effects are not included explicitly, since they require costly GW and Bethe–Salpeter calculations[82], and because the exciton binding energy is much smaller[83] than the defect level fluctuations. Excitations are introduced by promoting an electron from VBM to CBM, or a trap state for sub-bandgap excitation. Excitations above the bandgap relax rapidly, on a sub-picosecond timescale, by intraband relaxation through dense manifolds of states[84,85]. Charge trapping, de-trapping and recombination take tens of picoseconds to nanoseconds, and this timescale separation allows us to focus on the slow processes. The decoherence induced surface hopping method is used[86,87], as implemented in the PYthon Extension for Ab Initio Dynamics (PYXAID) package[88,89]. Several thousands of DISH trajectories are generated for each modeled process to obtain converged results.

Data availability

The data reported in the paper are available from the corresponding author upon reasonable request.

Code availability

The codes used in this paper are available from the corresponding author upon reasonable request.

Received: 24 October 2023; Accepted: 17 November 2024;
Published online: 11 January 2025

References

1. Butler, K. T., Sai Gautam, G. & Canepa, P. Designing interfaces in energy materials applications with first-principles calculations. *Npj Comput. Mater.* **5**, 19 (2019).
2. Barham, J. P. & König, B. Synthetic photoelectrochemistry. *Angew. Chem. Int. Ed.* **59**, 11732–11747 (2020).
3. Carusotto, I. et al. Photonic materials in circuit quantum electrodynamics. *Nat. Phys.* **16**, 268–279 (2020).
4. Li, Q. & Li, Z. Molecular packing: another key point for the performance of organic and polymeric optoelectronic materials. *Acc. Chem. Res.* **53**, 962–973 (2020).
5. Gao, Y., Zhong, C., Yang, S. A., Liu, K. & Lu, Z.-Y. Three-dimensional acetylenic modified graphene for high-performance optoelectronics and topological materials. *Npj Comput. Mater.* **7**, 109 (2021).
6. Dey, A. et al. State-of-the-art and prospects for halide perovskite nanocrystals. *ACS Nano* **15**, 10775–10981 (2021).
7. Xu, H. et al. Colossal switchable photocurrents in topological Janus transition metal dichalcogenides. *Npj Comput. Mater.* **7**, 31 (2021).
8. Liu, J., Li, Z., Zhang, X. & Lu, G. Unraveling energy and charge transfer in type-II van der Waals heterostructures. *Npj Comput. Mater.* **7**, 191 (2021).
9. Zheng, Q. et al. Ab initio nonadiabatic molecular dynamics investigations on the excited carriers in condensed matter systems. *Wiley Interdiscip. Rev. Comput. Mol. Sci.* **9**, e1411 (2019).
10. Smith, B. & Akimov, A. V. Modeling nonadiabatic dynamics in condensed matter materials: some recent advances and applications. *J. Phys. Condens. Matter* **32**, 073001 (2019).
11. Cheng, C., Zhu, Y., Zhou, Z., Long, R. & Fang, W.-H. Photoinduced small electron polarons generation and recombination in hematite. *Npj Comput. Mater.* **8**, 148 (2022).
12. Nelson, T. R. et al. Non-adiabatic excited-state molecular dynamics: theory and applications for modeling photophysics in extended molecular materials. *Chem. Rev.* **120**, 2215–2287 (2020).
13. Prezhdo, O. V. Modeling non-adiabatic dynamics in nanoscale and condensed matter systems. *Acc. Chem. Res.* **54**, 4239–4249 (2021).
14. Gao, Y., Jiang, X., Qiu, Z. & Zhao, J. Photoexcitation induced magnetic phase transition and spin dynamics in antiferromagnetic Mnps3 monolayer. *npj Comput. Mater.* **9**, 107 (2023).

15. Jankowska, J. & Sobolewski, A. L. Modern theoretical approaches to modeling the excited-state intramolecular proton transfer: an overview. *Molecules* **26**, 5140 (2021).
16. Giannini, S. & Blumberger, J. Charge transport in organic semiconductors: the perspective from nonadiabatic molecular dynamics. *Acc. Chem. Res.* **55**, 819–830 (2022).
17. Mandal, A. et al. Theoretical advances in polariton chemistry and molecular cavity quantum electrodynamics. *Chem. Rev.* **123**, 9786–9879 (2023).
18. Wang, L., Prezhdo, O. V. & Beljonne, D. Mixed quantum-classical dynamics for charge transport in organics. *Phys. Chem. Chem. Phys.* **17**, 12395–12406 (2015).
19. Liu, D. Y., Wang, B. P., Wu, Y. F., Vasenko, A. S. & Prezhdo, O. V. Breaking the size limitation of nonadiabatic molecular dynamics in condensed matter systems with local descriptor machine learning. *Proc. Nat. Acad. Sci. USA* **121**, e2403497121 (2024).
20. Frost, J. M. et al. Atomistic origins of high-performance in hybrid halide perovskite solar cells. *Nano Lett.* **14**, 2584–2590 (2014).
21. Li, K. et al. Origin of ferroelectricity in two prototypical hybrid organic–inorganic perovskites. *J. Am. Chem. Soc.* **144**, 816–823 (2022).
22. Stranks, S. D. & Snaith, H. J. Metal-halide perovskites for photovoltaic and light-emitting devices. *Nat. Nanotechnol.* **10**, 391–402 (2015).
23. Wang, F. et al. Switchable rashba anisotropy in layered hybrid organic–inorganic perovskite by hybrid improper ferroelectricity. *Npj Comput. Mater.* **6**, 183 (2020).
24. Manser, J. S., Christians, J. A. & Kamat, P. V. Intriguing optoelectronic properties of metal halide perovskites. *Chem. Rev.* **116**, 12956–13008 (2016).
25. Osei-Agyemang, E., Adu, C. E. & Balasubramanian, G. Ultralow lattice thermal conductivity of chalcogenide perovskite Cazrse3 contributes to high thermoelectric figure of merit. *Npj Comput. Mater.* **5**, 116 (2019).
26. Ghosh, S., Shankar, H. & Kar, P. Recent developments of lead-free halide double perovskites: a new superstar in the optoelectronic field. *Mater. Adv.* **3**, 3742–3765 (2022).
27. Huang, H. et al. Metal halide perovskite based heterojunction photocatalysts. *Angew. Chem.* **134**, e202203261 (2022).
28. Sun, P.-P., Bai, L., Kripalani, D. R. & Zhou, K. A new carbon phase with direct bandgap and high carrier mobility as electron transport material for perovskite solar cells. *Npj Comput. Mater.* **5**, 9 (2019).
29. Kojima, A., Teshima, K., Shirai, Y. & Miyasaka, T. Organometal halide perovskites as visible-light sensitizers for photovoltaic cells. *J. Am. Chem. Soc.* **131**, 6050–6051 (2009).
30. Kim, M. et al. Conformal quantum dot–Sno2 layers as electron transporters for efficient perovskite solar cells. *Science* **375**, 302–306 (2022).
31. Lee, M. M., Teuscher, J., Miyasaka, T., Murakami, T. N. & Snaith, H. J. Efficient hybrid solar cells based on meso-superstructured organometal halide perovskites. *Science* **338**, 643–647 (2012).
32. Nie, W. et al. Light-activated photocurrent degradation and self-healing in perovskite solar cells. *Nat. Commun.* **7**, 11574 (2016).
33. Frost, J. M., Whalley, L. D. & Walsh, A. Slow cooling of hot polarons in halide perovskite solar cells. *ACS energy Lett.* **2**, 2647–2652 (2017).
34. Munson, K. T., Kennehan, E. R., Doucette, G. S. & Asbury, J. B. Dynamic disorder dominates delocalization, transport, and recombination in halide perovskites. *Chem* **4**, 2826–2843 (2018).
35. Evans, T. J. et al. Competition between hot-electron cooling and large polaron screening in Cspbbr3 perovskite single crystals. *J. Phys. Chem. C* **122**, 13724–13730 (2018).
36. Butler, K. T., Frost, J. M. & Walsh, A. Band alignment of the hybrid halide perovskites Ch 3 Nh 3 Pbcl 3, Ch 3 Nh 3 Pbbr 3 and Ch 3 Nh 3 Pbi 3. *Mater. Horiz.* **2**, 228–231 (2015).
37. Cohen, A. V., Egger, D. A., Rappe, A. M. & Kronik, L. Breakdown of the static picture of defect energetics in halide perovskites: the case of the Br vacancy in Cspbbr3. *J. Phys. Chem. Lett.* **10**, 4490–4498 (2019).
38. Wang, B. et al. Electron-volt fluctuation of defect levels in metal halide perovskites on a 100 Ps time scale. *J. Phys. Chem. Lett.* **13**, 5946–5952 (2022).
39. Liu, D., Wu, Y., Vasenko, A. S. & Prezhdo, O. V. Grain boundary sliding and distortion on a nanosecond timescale induce trap states in Cspbbr 3: ab initio investigation with machine learning force field. *Nanoscale* **15**, 285–293 (2023).
40. Wu, Y. F. et al. Fluctuations at metal halide perovskite grain boundaries create transient trap states: machine learning assisted ab initio analysis. *Acs Appl. Mater. Interfaces* **14**, 55753–55761 (2022).
41. Tong, C.-J., Cai, X., Zhu, A.-Y., Liu, L.-M. & Prezhdo, O. V. How hole injection accelerates both ion migration and nonradiative recombination in metal halide perovskites. *J. Am. Chem. Soc.* **144**, 6604–6612 (2022).
42. Butler, K. T., Davies, D. W., Cartwright, H., Isayev, O. & Walsh, A. Machine learning for molecular and materials science. *Nat. Commun.* **559**, 547–555 (2018).
43. Oviedo, F., Ferres, J. L., Buonassisi, T. & Butler, K. T. Interpretable and explainable machine learning for materials science and chemistry. *Acc. Mater. Res.* **3**, 597–607 (2022).
44. Ramprasad, R., Batra, R., Pilania, G., Mannodi-Kanakkithodi, A. & Kim, C. Machine learning in materials informatics: recent applications and prospects. *Npj Comput. Mater.* **3**, 54 (2017).
45. Schmidt, J., Marques, M. R., Botti, S. & Marques, M. A. Recent advances and applications of machine learning in solid-state materials science. *Npj Comput. Mater.* **5**, 83 (2019).
46. Zhang, Y. & Ling, C. A strategy to apply machine learning to small datasets in materials science. *Npj Comput. Mater.* **4**, 25 (2018).
47. Antunes, L. M., Grau-Crespo, R. & Butler, K. T. Distributed representations of atoms and materials for machine learning. *Npj Comput. Mater.* **8**, 44 (2022).
48. Keith, J. A. et al. Combining machine learning and computational chemistry for predictive insights into chemical systems. *Chem. Rev.* **121**, 9816–9872 (2021).
49. Behler, J. Four generations of high-dimensional neural network potentials. *Chem. Rev.* **121**, 10037–10072 (2021).
50. Zhou, G., Lubbers, N., Barros, K., Tretiak, S. & Nebgen, B. Deep learning of dynamically responsive chemical Hamiltonians with semiempirical quantum mechanics. *Proc. Natl. Acad. Sci. USA* **119**, e2120333119 (2022).
51. Li, H. et al. Deep-learning density functional theory Hamiltonian for efficient ab initio electronic-structure calculation. *Nat. Comput. Sci.* **2**, 367–377 (2022).
52. Wang, B., Chu, W., Tkatchenko, A. & Prezhdo, O. V. Interpolating nonadiabatic molecular dynamics Hamiltonian with artificial neural networks. *J. Phys. Chem. Lett.* **12**, 6070–6077 (2021).
53. Wang, B., Chu, W. & Prezhdo, O. V. Interpolating nonadiabatic molecular dynamics Hamiltonian with inverse fast Fourier transform. *J. Phys. Chem. Lett.* **13**, 331–338 (2022).
54. Wang, B. P. et al. Interpolating nonadiabatic molecular dynamics Hamiltonian with bidirectional long short-term memory networks. *J. Phys. Chem. Lett.* **14**, 7092–7099 (2023).
55. Li, W. et al. Control of charge recombination in perovskites by oxidation state of halide vacancy. *J. Am. Chem. Soc.* **140**, 15753–15763 (2018).
56. Martí, A. et al. Production of photocurrent due to intermediate-to-conduction-band transitions: a demonstration of a key operating principle of the intermediate-band solar cell. *Phys. Rev. Lett.* **97**, 247701 (2006).
57. Forde, A. & Kilin, D. Defect tolerance mechanism revealed! influence of polaron occupied surface trap states on $CsPbBr_3$ nanocrystal photoluminescence: ab initio excited-state dynamics. *J. Chem. Theory Comput.* **17**, 7224–7236 (2021).
58. Ran, J. Y. et al. Halide vacancies create no charge traps on lead halide perovskite surfaces but can generate deep traps in the bulk. *J. Phys. Chem. Lett.* **14**, 6028–6036 (2023).
59. Li, W., She, Y. L., Vasenko, A. S. & Prezhdo, O. V. Ab initio nonadiabatic molecular dynamics of charge carriers in metal halide perovskites. *Nanoscale* **13**, 10239–10265 (2021).

60. Qiao, L., Fang, W.-H., Long, R. & Prezhdo, O. V. Elimination of charge recombination centers in metal halide perovskites by strain. *J. Am. Chem. Soc.* **143**, 9982–9990 (2021).
61. Liu, D. Y. et al. Compression eliminates charge traps by stabilizing perovskite grain boundary structures: an ab initio analysis with machine learning force field. *Chem. Mater.* **36**, 2898–2906 (2024).
62. Liu, L., Fang, W.-H., Long, R. & Prezhdo, O. V. Lewis base passivation of hybrid halide perovskites slows electron–hole recombination: time-domain ab initio analysis. *J. Phys. Chem. Lett.* **9**, 1164–1171 (2018).
63. Long, R., Fang, W. H. & Prezhdo, O. V. Strong interaction at the Perovskite/TiO_2 interface facilitates ultrafast photoinduced charge separation: a nonadiabatic molecular dynamics study. *J. Phys. Chem. C.* **121**, 3797–3806 (2017).
64. Shi, R., Vasenko, A. S., Long, R. & Prezhdo, O. V. Edge influence on charge carrier localization and lifetime in $Ch_3Nh_3PbBr_3$ Perovskite: Ab initio quantum dynamics simulation. *J. Phys. Chem. Lett.* **11**, 9100–9109 (2020).
65. Chu, W., Saidi, W. A., Zhao, J. & Prezhdo, O. V. Soft lattice and defect covalency rationalize tolerance of Β-Cspbi3 Perovskite solar cells to native defects. *Angew. Chem. Int. Ed.* **59**, 6435–6441 (2020).
66. Li, W., Vasenko, A. S., Tang, J. & Prezhdo, O. V. Anharmonicity extends carrier lifetimes in lead halide perovskites at elevated temperatures. *J. Phys. Chem. Lett.* **10**, 6219–6226 (2019).
67. Perdew, J. P., Burke, K. & Ernzerhof, M. Generalized gradient approximation made simple. *Phys. Rev. Lett.* **77**, 3865 (1996).
68. Kresse, G. & Joubert, D. From ultrasoft pseudopotentials to the projector augmented-wave method. *Phys. Rev. B* **59**, 1758 (1999).
69. Grimme, S., Antony, J., Ehrlich, S. & Krieg, H. A consistent and accurate ab initio parametrization of density functional dispersion correction (Dft-D) for the 94 Elements H-Pu. *J. Chem. Phys.* **132**, 154104 (2010).
70. Kresse, G. & Hafner, J. Ab initio molecular dynamics for liquid metals. *Phys. Rev. B* **47**, 558 (1993).
71. Zhang, L., Han, J., Wang, H., Saidi, W. & Car, R. End-to-end symmetry preserving inter-atomic potential energy model for finite and extended systems. *Adv. Neural Inform. Process. Syst.* **31**, 4436–4446 (2018).
72. Wang, H., Zhang, L., Han, J. & Weinan, E. Deepmd-Kit: a deep learning package for many-body potential energy representation and molecular dynamics. *Comput. Phys. Commun.* **228**, 178–184 (2018).
73. VandeVondele, J. et al. Quickstep: fast and accurate density functional calculations using a mixed Gaussian and Plane waves approach. *Comput. Phys. Commun.* **167**, 103–128 (2005).
74. VandeVondele, J. & Hutter, J. Gaussian basis sets for accurate calculations on molecular systems in gas and condensed phases. *J. Chem. Phys.* **127**, 114105 (2007).
75. Goedecker, S., Teter, M. & Hutter, J. Separable dual-space Gaussian pseudopotentials. *Phys. Rev. B* **54**, 1703 (1996).
76. Kingma, D. P. Adam: A Method for Stochastic Optimization. *arXiv preprint arXiv* (2014).
77. Thompson, A. P. et al. Lammps-a flexible simulation tool for particle-based materials modeling at the atomic, meso, and continuum scales. *Comput. Phys. Commun.* **271**, 108171 (2022).
78. Momma, K. & Izumi, F. Vesta: a three-dimensional visualization system for electronic and structural analysis. *J. Appl. Crystallogr.* **41**, 653–658 (2008).
79. Chu, W. et al. Accurate computation of nonadiabatic coupling with projector augmented-wave pseudopotentials. *J. Phys. Chem. Lett.* **11**, 10073–10080 (2020).
80. Chu, W. & Prezhdo, O. V. Concentric approximation for fast and accurate numerical evaluation of nonadiabatic coupling with projector augmented-wave pseudopotentials. *J. Phys. Chem. Lett.* **12**, 3082–3089 (2021).
81. Craig, C. F., Duncan, W. R. & Prezhdo, O. V. Trajectory surface hopping in the time-dependent Kohn-Sham approach for electron-nuclear dynamics. *Phys. Rev. Lett.* **95**, 163001 (2005).
82. Jiang, X. et al. Real-time *GW*-BSE investigations on spin-valley exciton dynamics in monolayer transition metal dichalcogenide. *Sci. Adv.* **7**, eabf3759 (2021).
83. D'Innocenzo, V. et al. Excitons versus free charges in organo-lead tri-halide perovskites. *Nat. Commun.* **5**, 3586 (2014).
84. Hedley, G. J. et al. Hot-hole cooling controls the initial ultrafast relaxation in methylammonium lead iodide perovskite. *Sci. Rep.* **8**, 8115 (2018).
85. Hu, J. G. et al. Reducing hot carrier cooling rate in metal halide perovskites through lead vacancies: time-domain ab initio analysis. *Inorg. Chem. Front.* **11**, 3950–3960 (2024).
86. Jaeger, H. M., Fischer, S. & Prezhdo, O. V. Decoherence-induced surface hopping. *J. Chem. Phys.* **137**, 22A545 (2012).
87. Liu, D. Y., Wang, B. P., Vasenko, A. S. & Prezhdo, O. V. Decoherence ensures convergence of non-adiabatic molecular dynamics with number of states. *J. Chem. Phys.* **161**, 064104 (2024).
88. Akimov, A. V. & Prezhdo, O. V. The pyxaid program for non-adiabatic molecular dynamics in condensed matter systems. *J. Chem. Theory Comput.* **9**, 4959–4972 (2013).
89. Akimov, A. V. & Prezhdo, O. V. Advanced capabilities of the pyxaid program: integration schemes, decoherence effects, multiexcitonic states, and field-matter interaction. *J. Chem. Theory Comput.* **10**, 789–804 (2014).

Acknowledgements

Support of the US National Science Foundation, grant CHE-2154367 is gratefully acknowledged. W.A.S. is grateful to the U.S. National Science Foundation (Award No. CSSI-2003808).

Author contributions

O.V.P. designed and supervised the project. W.A.S. designed the machine learning force field. B.W., W.C. and Y.W. performed the calculations and analyzed the results. B.W. and O.V.P. wrote the manuscript.

Competing interests

The authors declare no competing interests.

Additional information

Correspondence and requests for materials should be addressed to Oleg V. Prezhdo.